

Perturbation mapping of water leak in buried water pipes via laboratory validation experiments with high-frequency ground penetrating radar (GPR)

Wallace W.L. Lai*, Ray K.W. Chang, Janet F.C. Sham, K. Pang
Department of Land Surveying and Geo-informatics, The Hong Kong Polytechnic University

* email of corresponding author: wllai@polyu.edu.hk, and
phone number of corresponding author: (852) 3400 8960

Abstract

This paper studies the perturbation patterns of GPR images as a tool for water leakage detection in buried water pipes with laboratory experiments. Different perturbations patterns on GPR signals due to a water leak of metallic and PVC pipes buried in a sand box, were mapped and studied with controlled water injection and leak volume, as well as a fixed leak position in the pipes. These perturbation patterns of signal strength include the tale-tell signs of a central leak point and propagation of the radial wetting front vortex centered around the leak point at different injection times. These patterns, compared to the no-leak dry condition, were interpreted with the conventional principles of dielectric contrast and reflection coefficients, and the associated reflection and absorption mechanisms. It is believed that this set of data will serve as an image matching fingerprint to identify and map water leaks in the field.

Keywords: water leak, ground penetrating radar, water perturbation patterns.

1. Introduction

The unseen network of underground utilities is notably one of the few most complex man-made networks in any city. These indispensable networks include high-pressure water supply pipes, gas pipes and power cables; sewers and storm water drainage, telecommunication cables, and street lighting and traffic lighting cables. Compared to the obvious and visible damages in

infrastructures like bridges and roads, their existence and aging problems are seldom taken care of, until it fails and causes a bundle of problems such as gas explosion, road collapse due to subsurface wash-out, water leakage and seepage to the road surface, etc (Hao et al. 2012; Liu and Kleiner 2013; Metje et al. 2007). In congested cities located in hilly terrain like Hong Kong, the water transmission and distribution networks are probably the most problematic issues amongst all types of underground utilities. It is because the main distribution networks always operate under high pressure, which constantly causes underground water leaks and seepage (WSD, 2014). There is a significant amount of fresh water loss elsewhere, an example in Hong Kong is the implementation of various measures to reduce water loss from 25 percent in 2001 to 15 percent by 2015 through active leak control management (Kwan et al. 2009). A major portion of this loss is due to aging underground pipe network in the city, causing un-noticed subsurface washout, disturbance to everyday life when this leak turns to burst, waste money and precious natural resources.

To monitor water leak, it is customary to divide large area into smaller district metering area (DMA) (Charalambous, 2005; Savić and Ferrari, 2014) by observing the peculiar patterns in night flow (2-4 am) with noise logger and flow sensors (WSD, 2014). The patterns are subsequently confirmed by leak noise correlator (LNC) by correlating acoustic signals generated by two acoustic transmitters at two ends of a connected and pressurized water pipe (Gao et al. 2005; Hau et al. 2012). Another method is condition assessment of leaks directly by inserting sensors into the pipe, such as the Sahara System (Hau et al 2012).

LNC and pipe pigging are in fact two of the near-surface geophysical (NSG) methods which interpret the different types of wave and induction properties in materials. These methods are the

only way to detect water leakage in a pipeline because of its high resolution and yet nondestructive nature (Hao et al. 2012; Liu and Kleiner 2013; Metje et al. 2007). Amongst the family of NSG methods, ground penetrating radar (GPR) is an alternative and appear to be a promising, cost- and operator- efficient NSG method (Ayala-Cabrera et al. 2011; Nakhkash and Mahmood-Zadeh 2004; Stampolidis et al. 2003; Takahashi and Sato 2006). GPR surveys the subsurface from the ground by sending high frequency EM pulses to the subsurface and receiving the reflection echoes. When there exists a subsurface layer or an object with dielectric properties yielding sufficient dielectric contrast compared to that of the host materials, reflections go back to the receiving antenna and are registered as a waveform. With sophisticated signal processing, these waveforms across a volume of subsurface can be compiled to generate a 3D subsurface map to 'see through the unseen'.

There are three reasons for using GPR to map water seepage, leaks and bursts. Firstly, amongst non-metallic materials, water is the single most influential factor affecting radar wave's traveling velocity and reflection strength, and absorbing high-frequency portion in spectral content because of the mechanism of dielectric polarization (Glaser et al. 2012; Hugenschmidt and Loser 2008; Huisman et al. 2003; Klysz and Balayssac 2007; Lai et al. 2014; Lai et al. 2006; Lai et al. 2010; Lai et al. 2011a; Lai et al. 2011b; Lai et al. 2012). Secondly, by GPR, the internal condition of the subsurface in multiple dimensions can be unfolded efficiently and in very high resolution in milli-meter. It is because unlike acoustic methods such as acoustic emission or leak noise correlation methods, or electromagnetic induction methods (or pipe cable locating), GPR imaging does not require physical contact with any objects connecting the pipe, like valves. Compared with the seismic and low-frequency vibro-acoustics (Muggleton and Gao, 2011; Muggleton and Papandreou; 2014); Muggleton et al.; 2014), GPR does not require physical

excitation of the ground and its milli-meter resolution allows high-resolution imaging of the subsurface in urban congested underground. Lastly, GPR's wide frequency range matches different physical sizes/scales of structure thicknesses. For example, an antenna of 100-500MHz is suitable to study slopes in tens of meter scale, then 400-900MHz for seawalls and roads in meter scale, and 1000-3000MHz for underground utilities and buildings structures in centimeter scale. Results based on high-frequency (>1000MHz) GPR in scaled-down experiments in the lab can infer to the low-frequency GPR measurement in the field because of the insignificant velocity and attenuation dispersion across the GPR frequency range (Annan 2004). This advantage makes controllable and scaled-down water-leak experiments of utilities in roads, slopes and seawalls possible in lab, as reported in this paper. This approach allows the validation of the water-leak mapping exercise and observation of perturbation patterns in small scales, and paves the way of more complicated field work and image matching in larger scales for early warning of water leak.

There are few previous studies using laboratory experiments and numerical modeling to investigate the potential of detecting water leakage using GPR (Bimpas et al. 2010; Cataldo et al. 2014a; Cataldo et al. 2014b; Crocco et al. 2009; Demirci et al. 2012; Eyuboglu et al. 2013; Hunaidi et al. 2000; Nakhkash and Mahmood-Zadeh 2004; Stampolidis et al. 2003). It was suggested that a remote leakage detection approach using GPR is theoretically possible (Dong et al. 2012). These studies proved the possibility of GPR mapping on water leakage detection. Accuracy of the results may be refined and improved by advancing digital signal processing (Hasan 2012) and can further be extended to a detailed three-dimensional model (Dong et al. 2012). This paper therefore attempts to deal with these perspectives and recognize the tell-tale

signs of perturbation patterns created by controlled water leaks in water pipes (Cataldo et al. 2014a; Cataldo et al. 2014b; Crocco et al. 2009; Eyuboglu et al. 2013; Hunaidi et al. 2000; Hyun et al. 2007; Stampolidis et al. 2003) as image matching fingerprints.

2. Experimental setup and instrumentation

The pipe leak scenario was simulated in a small acrylic tank with dimension 885mm (L) x 660mm (W) x 630mm (D) (Figure 1). Injection of equal amount of water in setup 1 (metallic pipe) and setup 2 (PVC pipe) was controlled by a valve and water flowed from the L-shaped pipe to the soil through a pre-drilled hole at the center of both pipes. The amount of water injection is recorded in Table 1. One end of the pipe was sealed to ascertain that water only leaked through the pre-drilled hole, while the other end connected to the water valve and water hose. In each setup, the metallic and PVC pipes (length 106 cm, external diameter 38mm) were placed inside the box and covered with dry sand at a cover depth of 100mm to simulate the case of water leakage respectively. This scaled-down model simulates the similar scenario in actual case of full scale, where the water mains can be up to several meter deep. Injection in both setups was divided into five times, where radar measurements were done in between each time of injection. The amount of injected water in each setup is the same and is reported in Table 1. The only variable of each setup was the amount of water injection, while other factors (equipment, sand, pipe alignment, pipe materials, pipe size, etc.) were the same.

Data collections of the tests were performed in an orthogonal grid (Figure 2) by using a Geophysical Survey System Inc (GSSI)'s 1.6GHz structure mini and 2 GHz palm GPR antennae (Figure 3) which scale down the normal utility survey to a penetration depth about 20cm. The

advantage of this scaled-down setup aims not to involve a large volume of soil (in the order of meters) probed with low-frequency GPR (e.g. 400MHz), while the underlying physics is still sufficiently demonstrated. The grid was marked on a thin polypropylene plate. One-dimensional A-scans were laterally stacked to construct two-dimensional B-scan radargrams for further data processing and analysis to re-construct 3D slice images. There were a total of 11 GPR traverses parallel to the x-axis and another 7 traverses parallel to the y-axis. Signals were post-processed with the commercial software Reflexw for 2D signal processing and radargram display, an in-house program in LabVIEW for velocity measurement with hyperbolic fitting, and the commercial software GPR Slice for 3D slice image's visualization.

For 2D signal processing, adjustment of the drift of waveform was carried out by standard dewow and direct current (DC) shift, and referencing of the ground position in the waveform was done by time zero correction. The equipment gain and background of the signal were also removed to stand out the signals from the pipes and water leaks. Then for the GPR wave velocity measurement, reflected hyperbolas were extracted from the radargram and processed in an in-house developed LabVIEW program. The peak of each reflected A-scan was selected automatically by the program to form hyperbolas correspondent to the pipe. Hence these hyperbolas were used for calculating the velocities at each water injection time with equation [1].

Pythagoras theorem was used to estimate the travelled path of the waveform, based on a common-offset method, i.e. separation of receiver and transmitter is fixed and the antennas are held in a shield container. The relationship between the wave velocity (as a function of oblique or

normal positions of the antenna relative to the pipe x_i) and various parameters can be restructured as below and Figure 4:

$$v(x_i) = \frac{\sqrt{(D+r)^2 + \left(x_i - \frac{s}{2}\right)^2} + \sqrt{(D+r)^2 + \left(x_i + \frac{s}{2}\right)^2}}{t(x_i)} \dots\dots[1]$$

where ‘D’ is the cover depth of the pipe (i.e. 100mm in this setup), ‘r’ is the external radius of the pipe; ‘ x_i ’ is the horizontal distance of the antenna from any buried objects oblique to the normal position of the pipe; ‘ $t(x_i)$ ’ is the two way travel time of the reflection from the transmitting/receiving antennae to the target at any distance ‘ x ’; ‘s’ is the antenna separation which is fixed in common-offset methods. According to the manufacturer’s information, the values of ‘s’ are 40 mm and 58 mm for the 2GHz and 1.6GHz antenna respectively. Note also that this method does not work when x_i approaches 0, or close to where the antenna is normal to the pipe.

For 3D slice image visualization, any non-measured spaces (or simply ‘gap’) shown as point ‘i’ within a grid (Figure 5) defined by the GPR traverses were interpolated by the inverse square’s distance algorithm, which estimates the signal strength not covered by the traverses, as shown in equation [2].

$$\text{Estimated signal strength at point 'i' in Figure 5} = \sum_{i=1}^n w_i \times z_i ; w_i = \frac{1}{h_i^2} \dots\dots[2]$$

where h_i = distance from point ‘i’ and nearby grid points in GPR traverses within the search radius (i.e. 1.5 times grid spacing), as shown as the dotted lines in Figure 5; z = measured signal strength at nearby grid points in the GPR traverses. After interpolation, amplitude at every spatial

coordinate was normalized relative to the maximum and minimum amplitude over the amplitude distribution in the entire 3D cube space. As illustrated in Figure 6, left, absolute amplitude over 50% of the amplitude histogram was defined as white color. Those amplitudes under 50% were represented as a linear descending rainbow scale from red to blue for 3D visualization of the water leaks (Figure 6, right).

3. Data Analysis

Before and after each water injection, B-scan radargrams by the 1.6GHz and 2GHz GPR were collected immediately along the overlaid orthogonal grid. The traverses (Y3) perpendicular to, as well as the traverses (X5) parallel to the pipes were selected in Figure 7 (metallic pipe) and 6 (PVC pipe). These two traverses coincide with the exact location of the pre-drilled hole 100mm beneath leaking water and therefore they are of primary interest. All radargrams collected over the orthogonal grid were used to re-create slice scans (C-scan) at the surface of the sand (0ns), slightly above ($t-0.1ns$ and $t-0.2ns$), exactly at (t), and slightly below ($t+0.1ns$ and $t+0.2ns$) the peak reflection of the wavelet corresponding to the pipe location. This slice scans show not only the patterns at the pipe level but also the patterns immediately above and below the pipe level. Different C-scans making use of the 2G and 1.6GHz antennae, as well as metallic or PVC pipes in different times of injections, are illustrated in Figure 8 (metallic pipe). Most wave velocities of the wave in the case of PVC pipe are not available since accurate hyperbolic shapes were not recognizable, as shown in Figure 8.

1. Stage 1: No-leak/dry state

Initially before the water injection, the sand was dry and the pipe was rendered as perfect hyperbolic shapes in traverses perpendicular to the pipes (leftmost of 1st and 2nd row, Figures 7

and 8), or a horizontal straight reflector in traverses parallel to the pipe (leftmost of 3rd and 4th row, Figures 7 and 8). These clear reflections arrive at an earlier time (around 1.2ns) compared to those disturbed reflections of the later water injection times as shown in the second to last column of Figures 7-8. It is because dry soil does not polarize nor delay the incident GPR wave as much as the wet soil does, as evidenced by the measured fast GPR wave velocity (about 0.195-0.205 m/ns) in dry state compared to the slower measured velocity (about 0.07-0.13 m/ns) after water injection (Figure 9). Also, un-disturbed, strong, straight and vertical reflections of both metallic and PVC pipes are shown in the left column of slice C-scans in Figures 10 and 11. These magnitude and shape of reflection demonstrated the absence of water and the so-called no-leak state of the pipes. These phenomena illustrate the baseline of the experiments.

2. Stage 2: Co-existence of leak point and wetting front vortex after water injection

Starting from the 1st injection in the metallic pipe, the pipe reflections were still observable but highly disturbed. The arrival times were delayed from the initial 1.2ns, to 2.5 to 3ns, and the pipe reflections were largely attenuated in Figure 7. In the case of the PVC pipe, the reflection of the pipe was entirely blurred after the very 1st injection (Figure 8). It is because the dielectric contrast (and hence reflection coefficient) across the air-filled PVC ($\epsilon'=1$) and wet soil (5~16) is not as much as that between the wet soil ($\epsilon'=5\sim 16$) and the metal ($\epsilon'\rightarrow \infty$). After the 3rd injection, the partially saturated soil demonstrated an ever stronger attenuation pattern of the GPR wave since the leak point/drilled hole faced upward in the pipe (Figure 1) and the pathway of seepage was therefore headed towards the GPR antenna positions. A clear V-shape can be seen in these radargrams which drew the boundary of propagating wetting front centered around the leak point, as shown in Figure 12. Within the V-shape, the sand was wetted, more attenuated and vice

versa for the area outside the V-shape. In particular in the 1.6GHz radargrams (2nd row of Figures 7 and 8), few perturbations close to the surface (Figure 13) were observed and can be attributed to the sink holes (Figure 14) generated due to the propagation of the wetting front to the surface. The middle of which was saturated and finally sink holes were generated due to the wash-out of sand, which is evidenced by the multiple reverberations observed at times between 0-0.5ns and during the 3rd, 4th and 5th water injection. This phenomenon is observable in the 2GHz radargrams but not as clear as that in the 1.6GHz radargrams.

When the visualization is changed from radargram (B-scan) as vertical section, to a slice scan (C-scan) which portrays the energy distribution at a particular depth, the propagation of the wetting front's vortex in both metallic and PVC pipes become immediately apparent in Figures 10 and 11. In these two figures, blue color represents an area with a weak background reflection strength where no other object was buried. White or red color to the left (dry state or before water injection) denotes the strong reflection where the metallic (Figure 10) or the PVC (Figure 11) pipe was buried. In the case of a metallic pipe in Figure 10, the strong, white and isolated reflections to the top of the slice scans are due to the vertical part of the L-shaped metallic injection pipe. This reflection is absent in Figure 11 because the PVC pipe was used and its dielectric contrast with the hosting sand is not as large as in the metallic pipe. The rest of the perturbation patterns can then be interpreted with association to the effect of water injection and seepage through the leak point.

This perturbation pattern by a leak point can be interpreted with two mechanisms, namely reflection mechanism and absorption mechanism. The reflection mechanism of water

perturbation is highlighted in two areas during both the 1st and 2nd water injection: (1) intense water saturation at the leak point, as well as (2) radial propagation of the unsaturated wetting front distanced from and centered about the leak point. For (1), the sand is believed to be fully saturated yielding a slow GPR wave velocity (about 0.075m/ns) and high dielectric constant (about 16) in Figure 10. For (2), the wetting front represents a radial expansion effort of water seepage into the connected pores within the sand matrix. Areas sandwiched between the leak point and the wetting front manifested an area with significant attenuation because its partial saturation does not yield significant dielectric contrast against its saturated counterpart in the central leak point, nor the unsaturated wetting front. Hence, water in this unsaturated zone serves as purely an absorber of attenuated GPR wave rather than a reflector as happened in the leak point or wetting front.

3. Stage 3: Disappearance of the leak point but the radial wetting front vortex remains

In this stage, the leak point vanished but the wetting front is still clearly observable. The absorption mechanism (blue color) dominates the areas within the wetting front, whilst the reflection mechanism (red or white color in radial shape) governs the interface across the radial wetting front of the dry zone.

4. Stage 4: Complete absorption of leak point and wetting front signals

Few deeper C-scans at late water injection times (Figure 10) are rendered by mostly blue color. This phenomenon suggests that the original wetting front vortex fully extended beyond the boundary of the surveyed area, as a result the wetting front was no longer visible. In such case,

most surveyed areas were partially saturated and were undergoing the absorption mechanism explained in Stage 2.

4. Conclusions

Perturbation patterns due to a water leak in a metallic and a PVC buried water pipe were studied in this paper. Signatures or fingerprints of water leak at the top of the metallic and plastic pipes were successfully identified by recognizing the leak point and wetting front propagating towards the dry sand. Mechanisms of these two identifications were explained with differences of dielectric contrast and reflection coefficient at various water injection stages. The use of these confirmed GPR fingerprints as a basis to identify water leak in pressurized water supply pipes or drainage pipes in the cities is well expected. In reality, the major challenges will be the reinforcement bars contained in concrete pavement which would shield part of the wave transmission and reflection, and the neighbour underground utilities which affect the signal perturbation of water leaks from a particular water pipe. Scenarios of these challenges will be simulated in the underground utility survey laboratory in the university.

Acknowledgement

The authors would like to acknowledge the funding support of The Hong Kong Polytechnic University and the Research Grants Council (PolyU 5393/13E) and the two reviewers for providing constructive comments.

References

1. Annan, A. P. (2004). *Ground Penetrating Radar : Principles, Procedures & Applications*, Mississauga : Sensors & Softwares Inc., c2004, Mississauga.

2. Ayala-Cabrera, D., Herrera, M., Izquierdo, J., Pérez-García, R. (2011). "Location of Buried Plastic Pipes using Multi-Agent Support Based on GPR Images." *Journal of Applied Geophysics*, 75(4), 679-686.
3. Bimpas, M., Amditis, A., Uzunoglu, N. (2010). "Detection of Water Leaks in Supply Pipes using Continuous Wave Sensor Operating at 2.45 GHz." *Journal of Applied Geophysics*, 70(3), 226-236.
4. Cataldo, A., Persico, R., Leucci, G., De Benedetto, E., Cannazza, G., Matera, L., De Giorgi, L. (2014a). "Time Domain Reflectometry, Ground Penetrating Radar and Electrical Resistivity Tomography: A Comparative Analysis of Alternative Approaches for Leak Detection in Underground Pipes." *NDT&E International*, 62, 14-28.
5. Cataldo, A., De Benedetto, E., Cannazza, G., Giaquinto, N., Savino, M., Adamo, F. (2014b). "Leak Detection through Microwave Reflectometry: From Laboratory to Practical Implementation." *Measurement*, 47, 963-970.
6. Charalambous B. (2005). Experience in DMA redesign at water board of Lemesos, Cyprus, Proceedings of the IWA Specialised Conference Leakage, IWA, Halifax, Nova Scotia, Canada.
7. Crocco, L., Prisco, G., Soldovieri, F., Cassidy, N. J. (2009). "Early-Stage Leaking Pipes GPR Monitoring Via Microwave Tomographic Inversion." *Journal of Applied Geophysics*, 67(4), 270-277.
8. Demirci, S., Yigit, E., Eskidemir, I. H., Ozdemir, C. (2012). "Ground Penetrating Radar Imaging of Water Leaks from Buried Pipes Based on Back- Projection Method." *NDT&E International*, 47, 35-42.
9. Dong, L., Carnalla, S., Shinozuka, M. (2012). "GPR survey for pipe leakage detection: Experimental and analytical study." *Proceedings of Nondestructive Characterization for Composite Materials, Aerospace Engineering, Infrastructure, and Homeland Security*, 1-7.
10. Eyuboglu, S., Mahdi, H., Al-Shukri, H. (2013). "Detection of water leaks using ground penetrating radar." *Proceedings of 3rd International Conference on Applied Geophysics*.
11. Gao Y., Brennan M.J., Joseph P.F., Muggleton J.M., Hunaidi O. (2005). On the selection of acoustic/vibration sensors for leak detection in plastic water pipes, *Journal of Sound and Vibration*, 283, 927-941.
12. Glaser, D. R., Werkema, D. D., Versteeg, R. J., Henderson, R. D., Rucker, D. F. (2012). "Temporal GPR Imaging of an Ethanol Release within a Laboratory-Scaled Sand Tank." *Journal of Applied Geophysics*, 86(0), 133-145.
13. Hao, T., Rogers, C. D. F., Metje, N., Chapman, D. N., Muggleton, J. M., Foo, K. Y., Wang, P., Pennock, S. R., Atkins, P. R., Swingler, S. G., Parker, J., Costello, S. B., Burrow, M. P. N., Anspach, J. H., Armitage, R. J., Cohn, A. G., Goddard, K., Lewin, P. L., Orlando, G., Redfern, M. A., Royal, A. C. D., Saul, A. J. (2012). "Condition Assessment of the Buried Utility Service Infrastructure." *Tunnelling and Underground Space Technology*, 28(0), 331-344.
14. Hasan, A. E. (2012). "The use of ground penetrating radar with a frequency 1GHz to detect water leaks from pipelines." *Proceedings of Sixteenth International Water Technology Conference, IWTC 16 2012*, 1-6.
15. Huginschmidt, J., and Loser, R. (2008). "Detection of Chlorides and Moisture in Concrete Structures with Ground Penetrating Radar." *Materials and Structures*, 41(4), 785-792.
16. Huisman, J. A., Hubbard, S. S., Redman, J. D., Annan, A. P. (2003). "Measuring Soil Water Content with Ground Penetrating Radar: A Review." *Vadose Zone Journal*, 2, 476-491.

17. Hunaidi, O., Chu, W., Wang, A., Guan, W. (2000). "Detecting Leaks in Plastic Pipes." *American Water Works Association*, 92(2), 82.
18. Hyun, S., Jo, Y., Oh, H., Kim, S., Kim, Y. (2007). "The Laboratory Scaled-Down Model of a Ground-Penetrating Radar for Leak Detection of Water Pipes." *The Laboratory Scaled-Down Model of a Ground-Penetrating Radar for Leak Detection of Water Pipes*, 18(9), 2791-2799.
19. Klysz, G., and Balayssac, J. -. (2007). "Determination of Volumetric Water Content of Concrete using Ground-Penetrating Radar." *Cement and Concrete Research*, 37(8), 1164-1171.
20. Kwan S.Y., Shou Stephanus, Kimshaiyong Tanin, Sathiasothy Sherine and Chan Kennie (2009). Pressure Management – A Strategic Measure to Reduce Non-Revenue Water in Hong Kong, *Water Practice & Technology* 4: 4.
21. Lai, W. L., Kind, T., Kruschwitz, S., Wostmann, J., Wiggenhauser, H. (2014). Spectral Absorption of Spatial and Temporal Ground Penetrating Radar Signals by Water in Construction Material." *NDT&E International*. 67, 55-63.
22. Lai, W. L., Kou, S. C., Poon, C. S. (2012). "Unsaturated Zone Characterization in Soil through Transient Wetting and Drying using GPR Joint Time–frequency Analysis and Grayscale Images." *Journal of Hydrology*, 452–453(0), 1-13.
23. Lai, W. L., Kind, T., Wiggenhauser, H. (2011a). "Using Ground Penetrating Radar and Time- Frequency Analysis to Characterize Construction Materials." *NDT&E International*, 44(1), 111-120.
24. Lai, W. L., Kind, T., Wiggenhauser, H. (2011b). "Frequency-Dependent Dispersion of High-Frequency Ground Penetrating Radar Wave in Concrete." *NDT&E International*, 44(3), 267-273.
25. Lai, W. L., Kind, T., Wiggenhauser, H. (2010). "A Study of Concrete Hydration and Dielectric Relaxation Mechanism using Ground Penetrating Radar and Short-Time Fourier Transform." *Eurasip Journal On Advances In Signal Processing*, 1-14.
26. Lai, W. L., Tsang, W. F., Fang, H., Xiao, D. (2006). "Experimental Determination of Bulk Dielectric Properties and Porosity of Porous Asphalt and Soils using GPR and a Cyclic Moisture Variation Technique." *Geophysics*, 71(4), K93-K102.
27. Liu, Z., and Kleiner, Y. (2013). "State of the Art Review of Inspection Technologies for Condition Assessment of Water Pipes." *Measurement*, 46(1), 1-15.
28. Muggleton J.M., Brennan M.J., Gao Y. (2011). Determining the location of buried plastic water pipes from measurements of ground surface vibration, *Journal of Applied Geophysics*, 75, 54-61.
29. Muggleton J.M., Brennan M.J., Rogers C.D.F. (2014). Point vibration measurements for the detection of shallow-buried objects, *Tunnelling and Underground Space Technology*, 39, 27-33.
30. Muggleton J.M. and Papandreou B. (2014) A shear wave ground surface vibration technique for the detection of buried pipes, *Journal of Applied Geophysics*, 106, 164–172.\
31. Metje, N., Atkins, P. R., Brennan, M. J., Chapman, D. N., Lim, H. M., Machell, J., Muggleton, J. M., Pennock, S., Ratcliffe, J., Redfern, M., Rogers, C. D. F., Saul, A. J., Shan, Q., Swingler, S., Thomas, A. M. (2007). "Mapping the Underworld – State-of-the-Art Review." *Tunnelling and Underground Space Technology*, 22(5–6), 568-586.

32. Nakhkash, M., and Mahmood-Zadeh, M. R. (2004). "Water leak detection using ground penetrating radar." *Proceedings of the 10th International Conference on Ground Penetrating Radar (GPR 2004)*, , 525-528.
33. Pennock S.R., Atkins P.R., Swingler S.G., Parker J., S.B. Costello, M.P.N. Burrow, J.H. Anspach, R.J. Armitage, A.G. Cohn, K. Goddard, P.L. Lewin, G. Orlando, M.A. Redfern, A.C.D. Royal, A.J. (2012) Saul. Condition assessment of the buried utility service infrastructure, *Tunnelling and Underground Space Technology*, 28, 331–344.
34. Savić D. and Ferrari G. (2014) Design and performance of district metering areas in water distribution systems, *Procedia Engineering* 89 1136.
35. Stampolidis, A., Soupios, P., Vallianatos, F., Tsokas, G. N. (2003). "Detection of leaks in buried plastic water distribution pipes in urban places—a case study." *Proceedings of the 2nd International Workshop on Advanced Ground Penetrating Radar (IWAGPR2003)*, Delft, The Netherlands, 120-124.
36. Takahashi, K., and Sato, M. (2006). "A novel inversion of cross-hole radar data for location of buried pipes." *Proceedings of the 11th International Conference on Ground Penetrating Radar (GPR 2006)*
37. Water Supplies Department (2014) Annual Report 2013/14 of the Water Supplies Department HKSAR Government,
http://www.wsd.gov.hk/filemanager/common/annual_report/2013_14/rpt1314.pdf

Injection times	Volume of injected water (m ³)
--	0
1st	0.0022
2nd	0.0028
3rd	0.0044
4th	0.0060
5th	0.0092

Table 1 Volume of injected water in each injection times

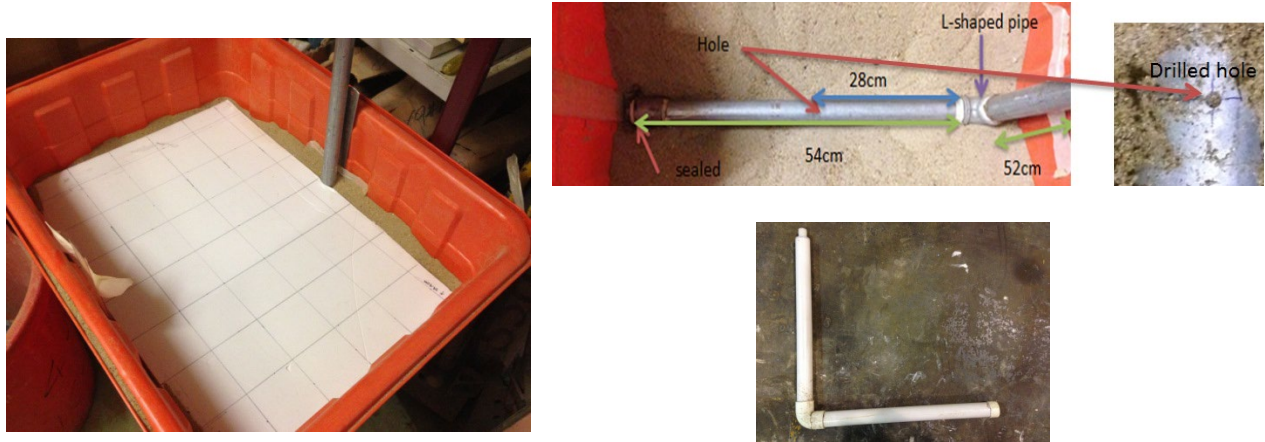


Figure 1 Acrylic tank sized 885 (L) x660(W) x 630 (D)(mm) that houses the steel and PVC pipes

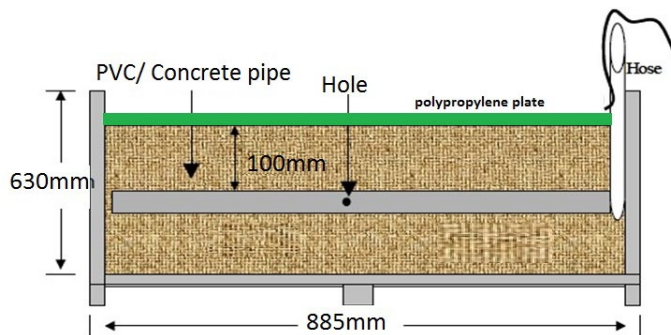
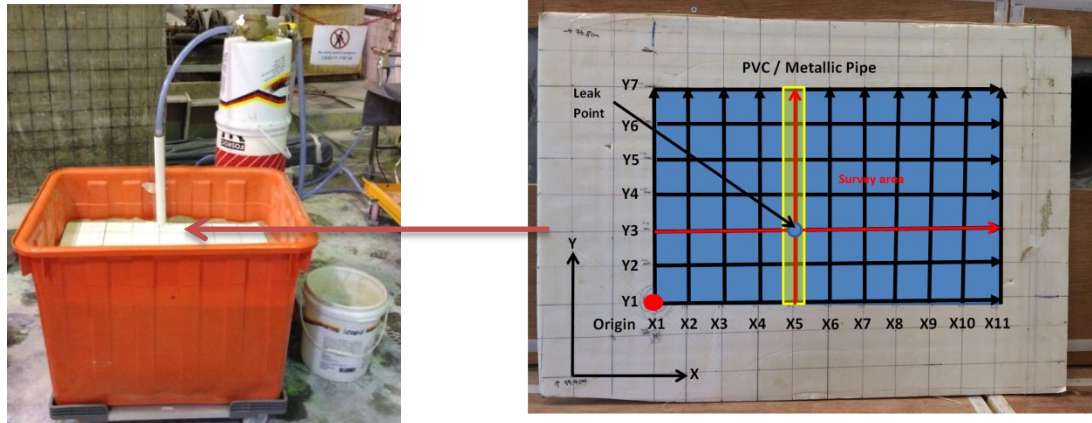


Figure 2 Experimental setup (top left), the overlaid grid (top right) and section of the acrylic tank



Figure 3 GSSI 2GHz Palm antenna (left) and 1.6GHz Structure Mini GPR

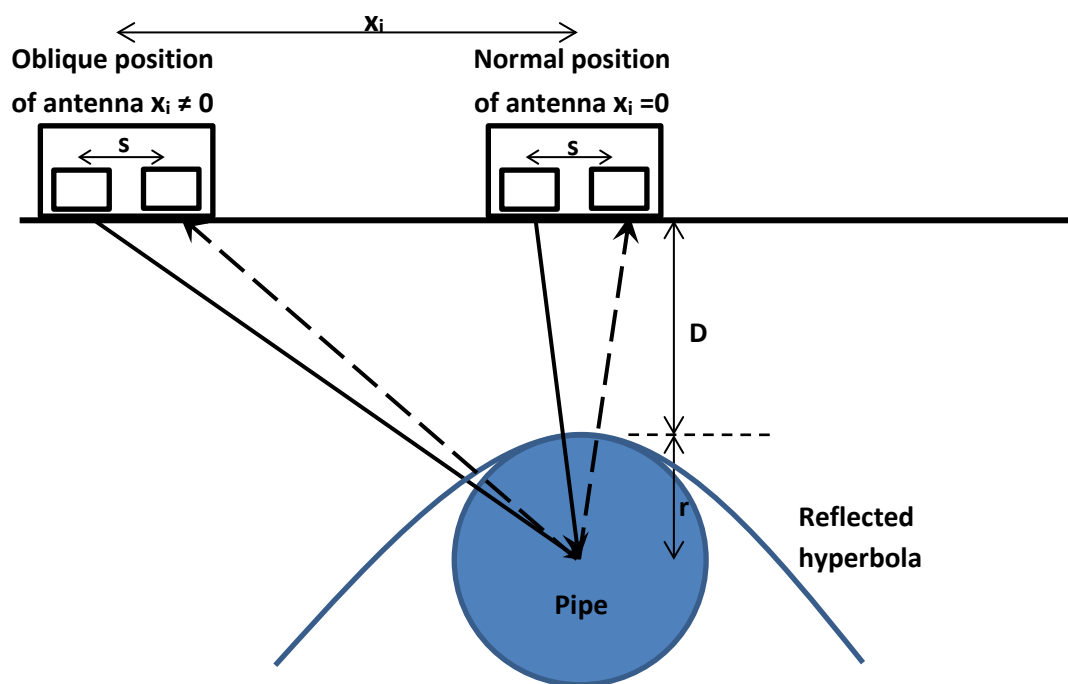


Figure 4 Geometry of wave transmission and reflection from the antenna to the pipe

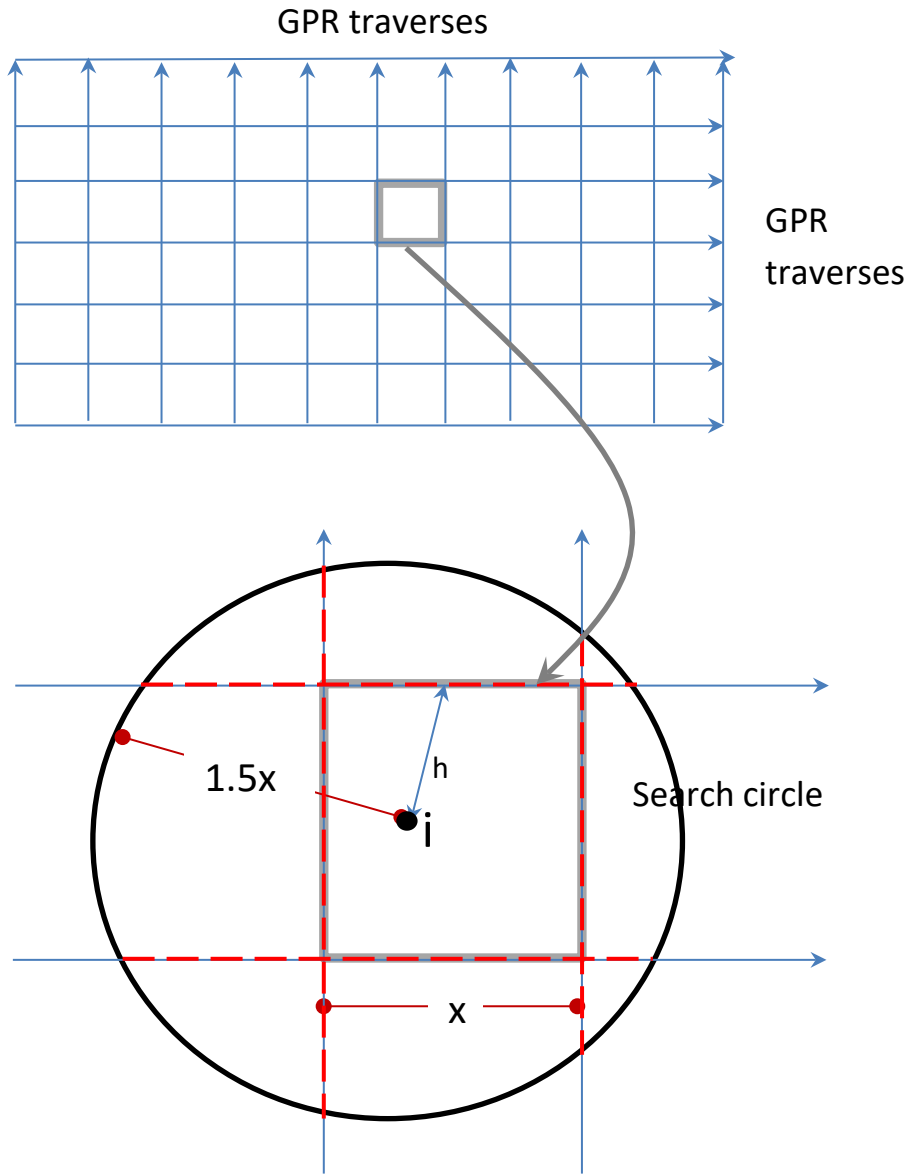


Figure 5 Interpolation of amplitude within a GPR grid

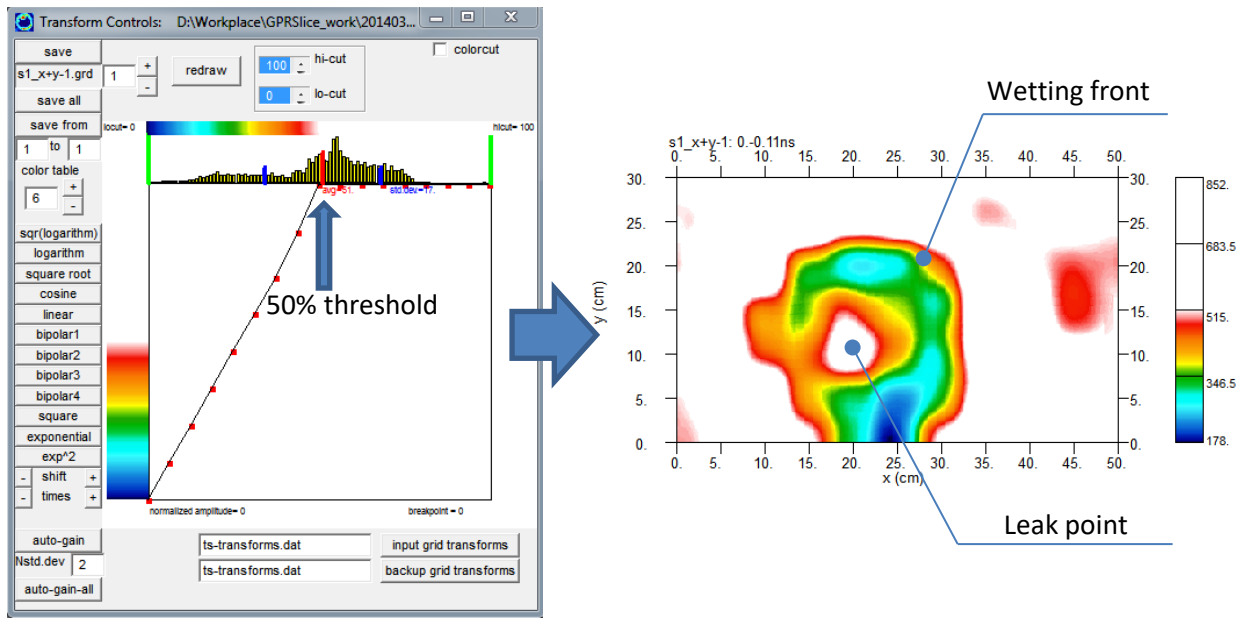
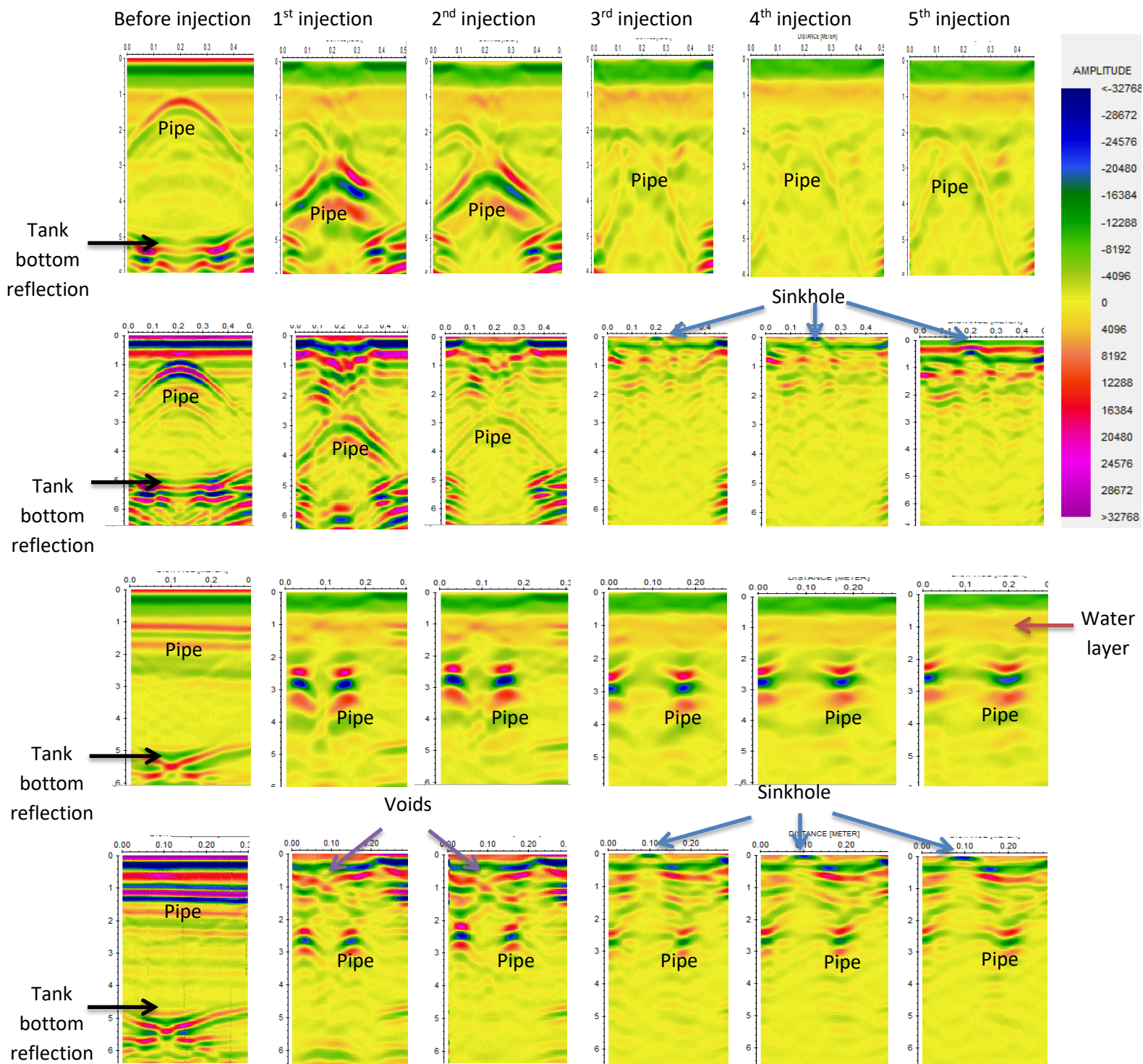
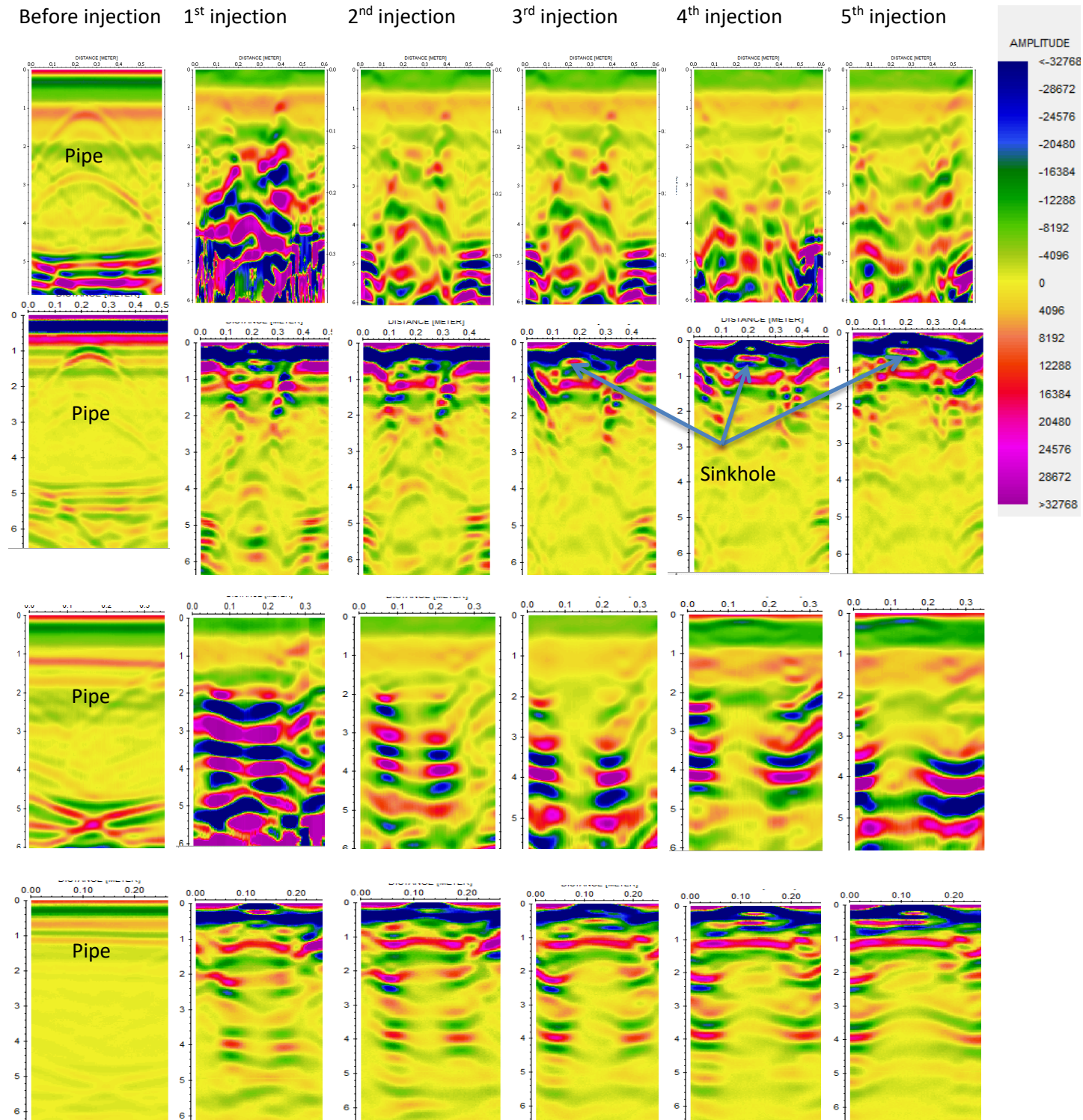


Figure 6 Amplitude normalization for 3D slice scans



Remarks: 1st row: 2GHz antenna, traverse Y3 perpendicular to the pipe; 2nd row: 1.6GHz antenna, traverse Y3 perpendicular to the pipe; 3rd row: 2GHz antenna, traverse X5 parallel to the pipe; 4th row: 1.6GHz, antenna traverse X5 perpendicular to the pipe)

Figure 7 Radargrams collected at different times of water injection, different antenna frequencies and perpendicular/parallel traverses over the **metallic pipe**



Remarks: 1st row: 2GHz antenna, traverse Y3 perpendicular to the pipe; 2nd row: 1.6GHz antenna, traverse Y3 perpendicular to the pipe; 3rd row: 2GHz antenna, traverse X5 parallel to the pipe; 4th row: 1.6GHz, antenna traverse X5 perpendicular to the pipe)

Figure 8 Radargrams collected at different times of water injection, different antenna frequencies and perpendicular/parallel traverses over the **PVC pipe**

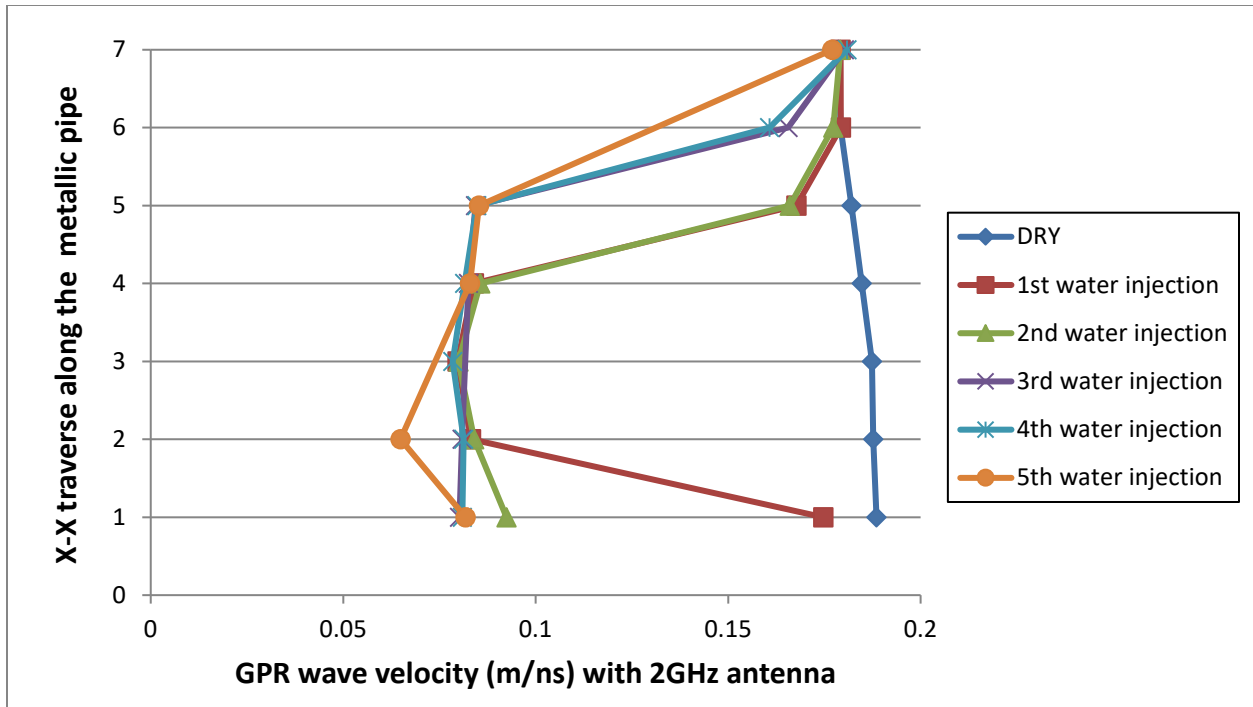


Figure 9a GPR wave velocity with 2GHz antenna

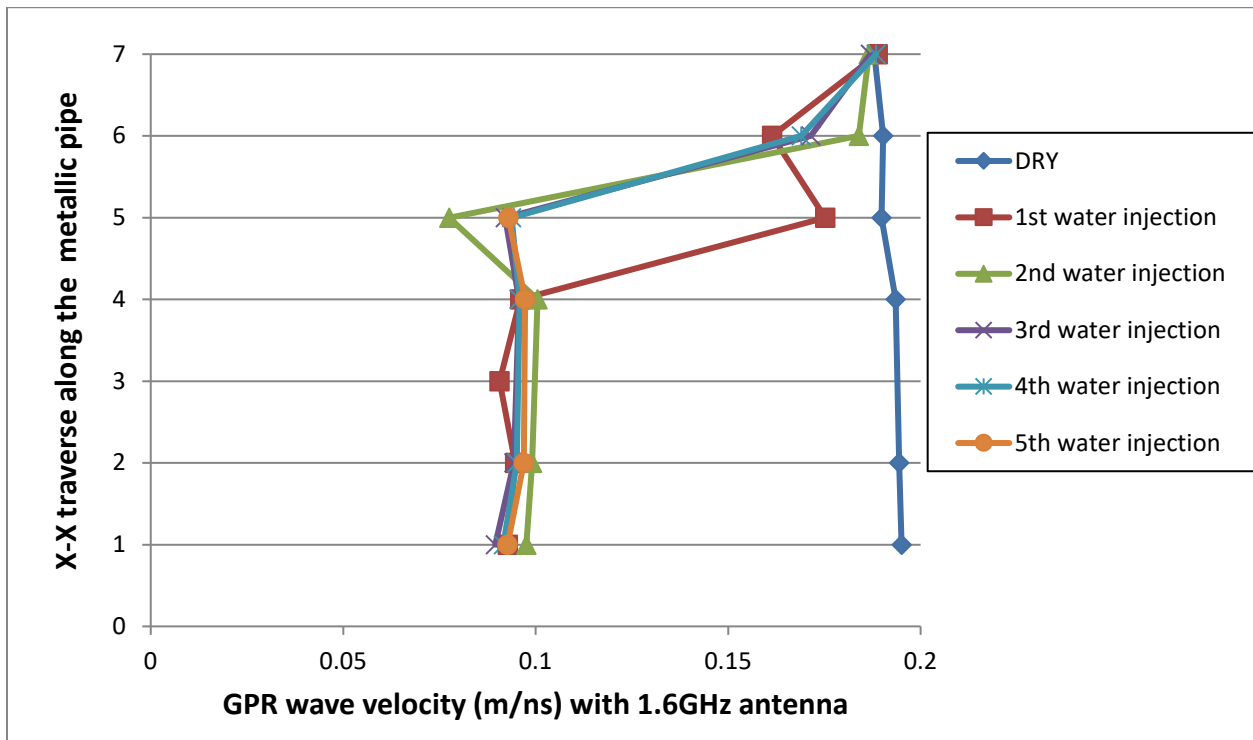


Figure 9b GPR wave velocity with 1.6GHz antenna

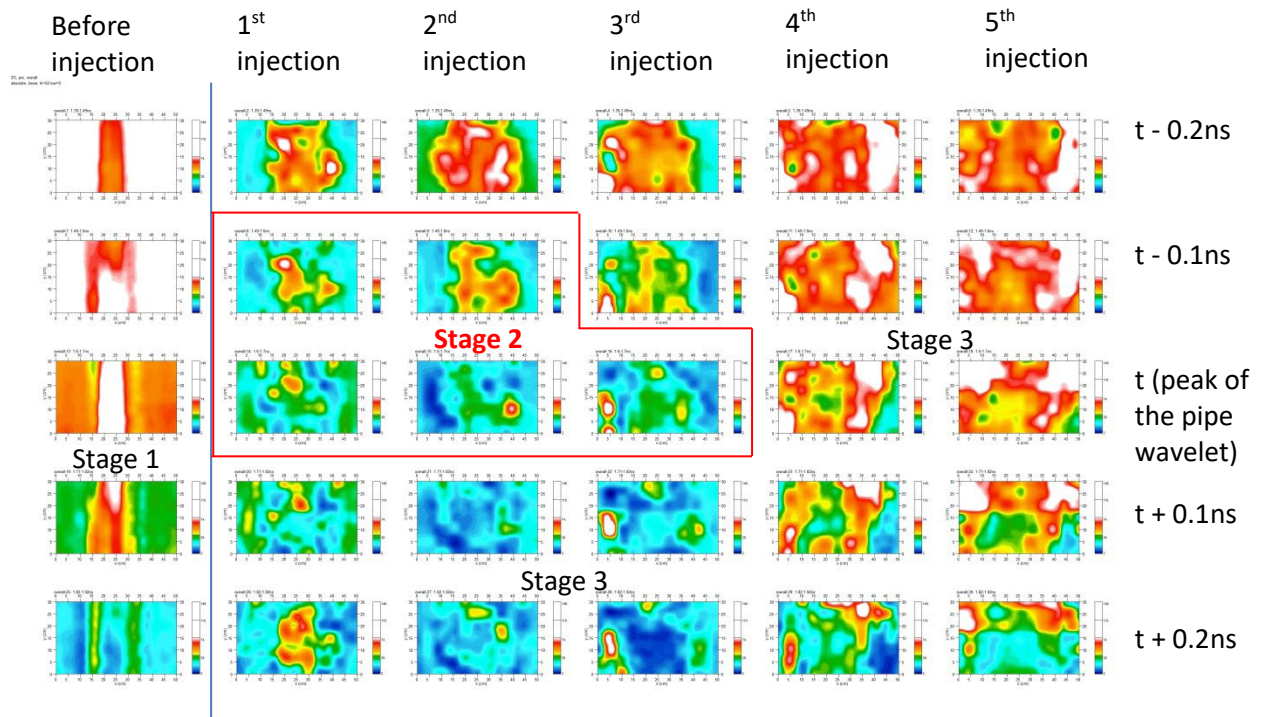


Figure 11a 3D visualization (with 2GHz antenna) at different stages of water injection in the **PVC pipe**

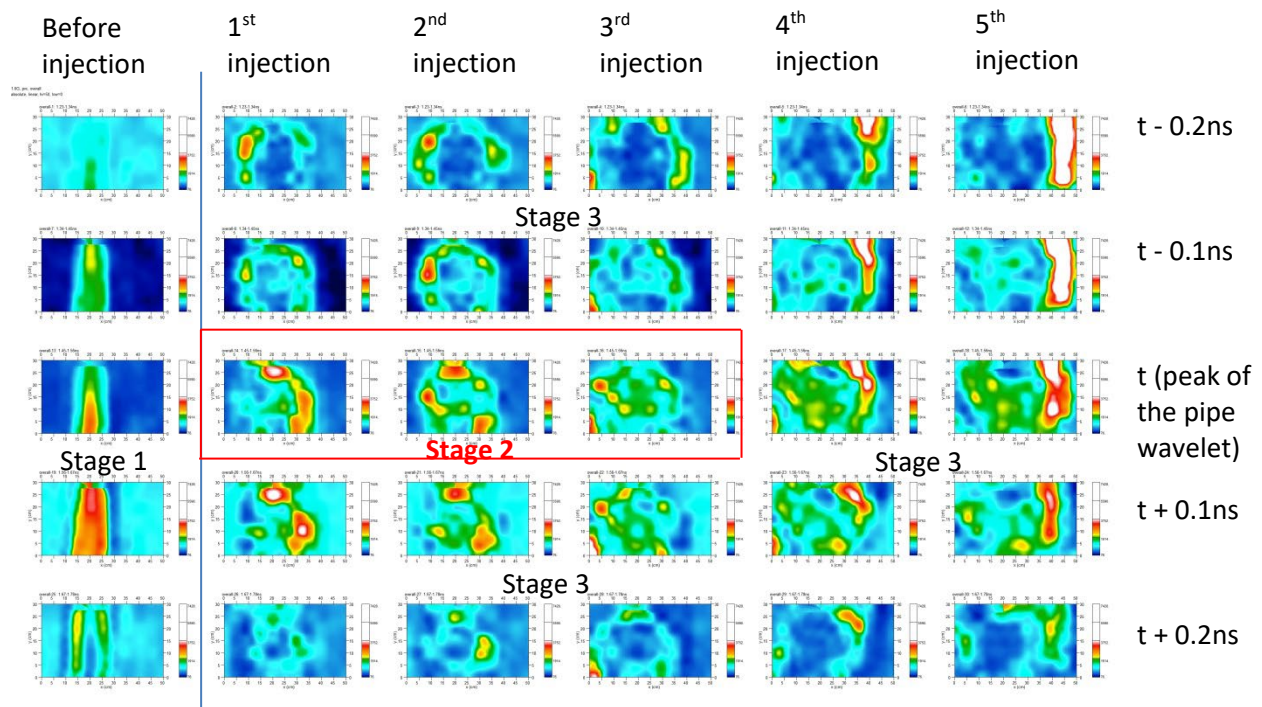


Figure 11b 3D visualization (with 1.6GHz antenna) at different stages of water injection in the **PVC pipe**

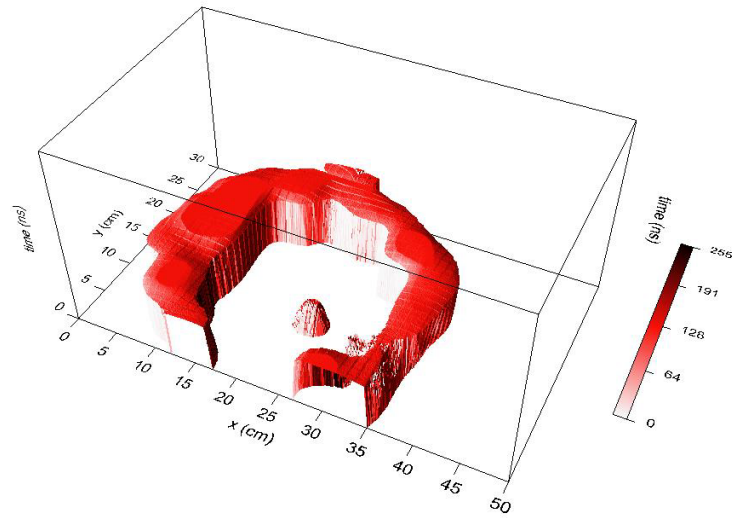


Figure 12 Isothermal representation of water leak point and wetting front of the PVC pipe during the 2nd water injection measured by 1.6GHz GPR

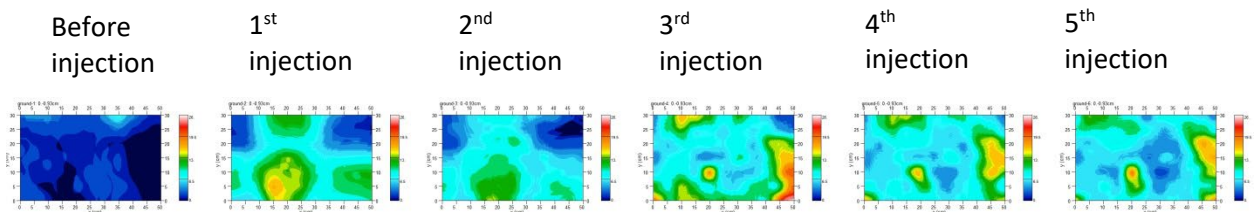


Figure 13a 3D visualization (with 2GHz antenna) at the sand surface in the setup with metallic pipe

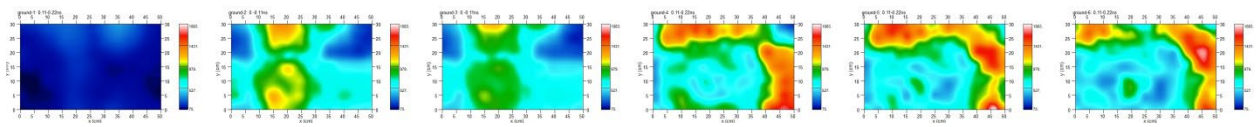


Figure 13b 3D visualization (with 1.6GHz antenna) at the sand surface in the setup with metal pipe

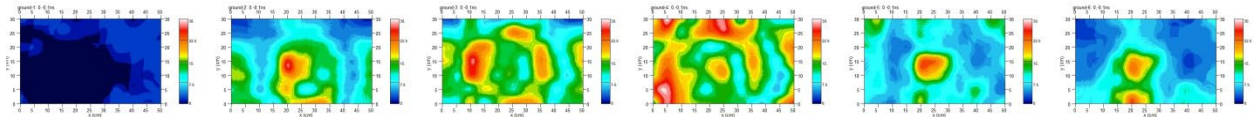


Figure 13c 3D visualization (with 2GHz antenna) at the sand surface in the setup with PVC pipe

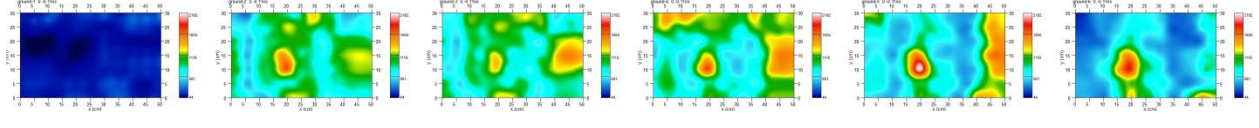


Figure 13d 3D visualization (with 1.6GHz antenna) at the sand surface in the setup with PVC pipe

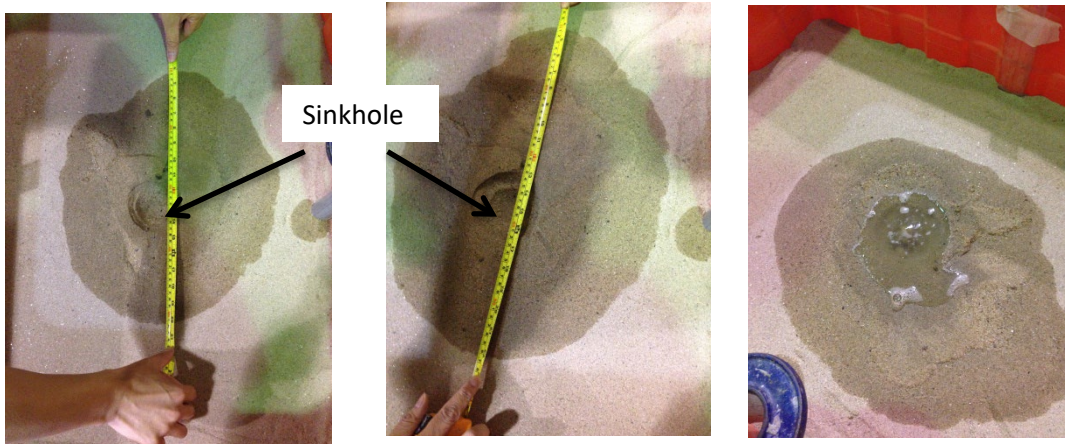


Figure 14 Formation of sinkholes after 3rd, 4th and 5th water injection